NAR Molecular Medicine, 2025, **2**, ugaf012
https://doi.org/10.1093/narmme/ugaf012
Advance access publication date: 5 May 2025
Standard Article

The role of RNA in the nanoscale organization of α-synuclein phase separation

Sabrina Zappone[1,2], **Eleonora Perego**[1], **Jakob Rupert**[3,4,5], **Elsa Zacco**[3], **Eli Slenders**[1], **Gian Gaetano Tartaglia**[3,4], **Giuseppe Vicidomini**[1,*]

[1]Molecular Microscopy and Spectroscopy, Istituto Italiano di Tecnologia, Via Enrico Melen 83 Bldg. B, 16152 Genoa, Italy
[2]Dipartimento di Informatiche, Bioingegneria, Robotica e Ingegneria dei Sistemi, University of Genoa, Via All'Opera Pia 13, 16145 Genoa, Italy
[3]RNA Systems Biology, Istituto Italiano di Tecnologia, Via Enrico Melen 85 Bldg. B, 16152 Genoa, Italy
[4]Department of Biology and Biotechnologies "C. Darwin," Sapienza University of Rome, Piazzale Aldo Moro, 00185 Rome, Italy
[5]Present address: Laboratory of Molecular Neuroscience, German Center for Neurodegenerative Diseases, Venusberg-Campus 1/99, 53127 Bonn, Germany

[*]To whom correspondence should be addressed. Email: giuseppe.vicidomini@iit.it

Abstract

The cellular accumulation of α-synuclein (aS) aggregates is a hallmark of several neurodegenerative diseases. Recent studies suggest that the aberrant transition of monomeric aS into solid-like aggregates may occur through an intermediate liquid-like state, where the protein partitions between dense and dilute phases. Although aS is not typically recognized as an RNA-binding protein, it can bind RNA under aggregation conditions, but its impact on aS liquid-like phases remains unexplored. Employing a combination of fluorescence spectroscopy techniques, we investigated aS mobility in both phases in the presence of RNA. Our analysis revealed the formation of nanoclusters involved in initiating phase separation and uncovered heterogeneity within the dense phase, discovering that aS molecules exist in two distinct mobility states. Additionally, we demonstrated that RNA induces morphological changes and promotes the liquid-to-solid transition of aS dense phase. These findings underscore the active role of RNA in modulating aS phase transitions.

Graphical abstract

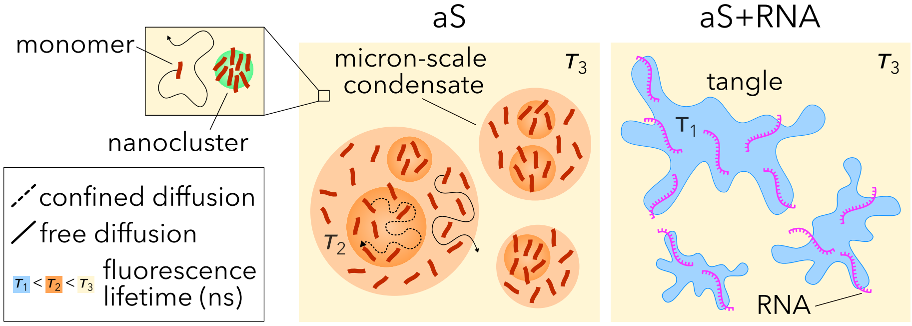

Introduction

Protein misfolding and aggregation, along with the associated loss of function, are hallmark features of several human disorders. Misfolded proteins typically aggregate into fibrillar structures known as amyloids [1]. While the amyloidogenesis of aggregation-prone proteins, such as amyloid β and α-synuclein (aS), has been extensively studied and characterized *in vitro* [2–4], the precise mechanisms governing these processes within the cellular context have initially remained less clear. In recent years, protein aggregation has been increasingly linked to liquid–liquid and liquid-to-solid phase transitions [5]. Liquid–liquid phase separation (LLPS) is a thermodynamically driven process whereby biomolecules self-organize into a dense liquid-like phase by establishing weak intermolecular interactions, co-existing with a surrounding dilute liquid-like phase [3]. The accumulation of molecules in the dense phase gives rise to micron-sized condensates, often referred to as membrane-less organelles (MLOs). MLOs play critical roles in cellular organization, enabling spatial and temporal tuning of reactions, sequestering potentially toxic molecules, or compartmentalizing cellular content [6].

Among the many proteins capable of undergoing such phase transitions, aS is an intrinsically disordered protein abundantly expressed in mammalian cells [7]. It has been asso-

Received: January 2, 2025. **Revised:** April 7, 2025. **Editorial Decision:** April 8, 2025. **Accepted:** May 3, 2025

ciated with various cellular processes, including synaptic vesicle trafficking, exocytosis, and DNA repair [7–9]. Of particular interest is its involvement in a group of neurodegenerative diseases collectively known as synucleopathies [10]. The pathological transition of aS from a soluble, monomeric state to an insoluble, irreversible state results in the accumulation of amyloid aggregates within cells. This phenomenon, known as liquid-to-solid transition, has long been accepted as the pathological pathway behind the deposition of aS monomers into amyloid aggregates [11]. More recently, LLPS and the subsequent maturation of liquid-like condensates into solid-like aggregates have emerged as a potential alternative pathological pathway [12]. Indeed, the high local concentration and confinement of molecules inside liquid-like condensates may facilitate primary nucleation and formation of solid aggregates under physiological conditions, a process further exacerbated by the uptake of pre-aggregated forms of aS [13, 14].

The aS phase transitions are significantly influenced by its interactions with various molecular partners, including proteins and nucleic acids [15, 16]. In fact, aS has been found in several multi-component MLOs in living cells, such as synaptic condensates [17] and processing bodies [18]. Apart from consisting of a number of different proteins, processing bodies are also enriched by substantial quantities of RNA, a molecule that plays pivotal role in the initiation and regulation of protein phase separation [19, 20]. Despite this, the effect of RNA in modulating aS phase transition remains incompletely understood. Most studies on aS phase separation have focused on its interaction with polynucleotides, such as poly(U) and poly(A). On one hand, poly(A) promotes the recruitment of aS on the condensate surface and accelerates its aggregation [21]. On the other hand, the aS fibril growth slows down in cationic peptide/poly(U) condensates due to the weak binding between poly(U) or peptides and aS monomers, oligomers, or fibrils [22]. Recently, specific interactions between aS and G-quadruplex RNA structures have been reported both *in vitro* and in cells, with G-quadruplex RNA shown to accelerate both aS liquid–liquid and liquid-to-solid phase transitions [23]. In contrast, misfolded and aggregated forms of aS exhibit an enhanced RNA-binding propensity, sequestering RNA molecules within aggregates [24]. Nevertheless, there is little evidence on how RNA can influence aS LLPS across nano- and microscale dimensions, or how such interactions contribute to pathological liquid-to-solid phase transitions. Recent studies suggest that the ability to undergo LLPS is not exclusive to the components of MLOs but occurs at a wide range in the cellular proteome [25] and a much lower scale than the micrometer scale [26]. Nanoscale condensates, also termed nanoclusters, have been identified as critical intermediates in the aS phase transitions [27]. These nanoclusters rapidly form in solution and persist even in the presence of macro-condensates, suggesting that LLPS may underline both aggregate formation and propagation [27]. Even though the phase separation of certain proteins can be regulated or disrupted at the nanocluster level [26], their impact on aS LLPS, particularly in relation to RNA, has not been investigated yet.

The investigation of LLPS systems has been predominantly focused on the dense phase. However, characterizing the dilute phase is fundamental for achieving a comprehensive understanding of these systems. This task poses significant technical challenges due to the inherent heterogeneity of the dilute phase and the potential formation of nanoclusters. Phase-separated systems have been conventionally studied using several methods, such as mass spectrometry [28], dynamic light scattering [29], nuclear magnetic resonance spectroscopy [30], and fluorescence microscopy techniques. While fluorescence confocal microscopy imaging has been extensively used for visualizing macro-condensates, it suffers from poor temporal (in terms of frame rate) and spatial resolution for quantifying the diffusivity of sub-diffraction-sized species such as nanoclusters. Fluorescence recovery after photobleaching (FRAP), typically implemented in a confocal laser scanning microscope, is widely used for characterizing intra-condensate diffusivity. However, FRAP measurements are often difficult to interpret as they depend on the optical system, laser power, and sample geometry [31]. They are mostly suitable for investigating the immobile fraction or very slow-moving molecules, making FRAP ineffective for studying the fast mobility in the dilute phase. Phase-separating proteins like aS show diverse temporal diffusivities, with very fast movement in the dilute phase and slower movement in the dense phase. As a result, relying solely on FRAP does not reveal all the underlying phenomena.

These limitations can partially be overcome by fluorescence fluctuation-based methods. Among them, fluorescence correlation spectroscopy (FCS) measures the mobility of the molecules by statistically analyzing the temporal correlation of fluctuations in fluorescence intensity [32]. To retrieve diffusion properties with FCS, molecules must move within a well-defined observation volume, such as one created by focusing a laser beam in a confocal microscope. FCS has already been applied to various LLPS scenarios, including identifying nanoclusters in the phase-separated system of pyrenoid [33] and amyloid [34] proteins. Both cases demonstrated that, due to its high single-molecule sensitivity, FCS is a suitable method for studying molecular interactions in nano- and macro-condensates.

While valuable for characterizing molecular species based on their different mobility, conventional FCS cannot distinguish the spatial heterogeneity inherent in LLPS systems. Spot-variation FCS (svFCS) addresses this limitation by performing FCS measurements with increasing observation volumes. This FCS variant allows for the determination of both molecular diffusion coefficients and movement types within the sample, thereby resolving heterogeneity in the molecular process investigated [35].

Here, we enhance conventional confocal FCS measurements by replacing the typical single-element detector of confocal microscopy, such as a photomultiplier or a single-photon avalanche diode (SPAD), with a SPAD array detector [36]. The array detector preserves the spatial distribution of the fluorescent signal generated by the observation volume within the sample, which would otherwise be lost with a single-element detector. This spatial information allows for a straightforward and instantaneous implementation of svFCS [37]. Moreover, the single-photon timing capability of each SPAD element facilitates photon time-tagging recording, which allows for sampling of the fluorescence signal photon-by-photon and with high temporal precision (down to the sub-nanosecond scale) [38]. This high temporal precision allows for the quantification of fluorescence lifetime changes. In the context of phase transitions, fluorescence lifetime has proven valuable in distinguishing molecular packing densities of proteins within MLOs [39–41] as well in studying the aggregation process of amyloidogenic proteins [42–44].

We have already shown that this suite, referred to as photon-resolved microscopy [38, 45], facilitates analysis across spatial scales from micrometers to nanometers and temporal scales from seconds to nanoseconds, enabling multiplexed analysis of condensate mobility with a single measurement [40]. The simultaneity and relatively short duration (tens of seconds) of the measurements guarantee reduced complexity and lower phototoxicity while preserving temporal heterogeneity.

By employing this platform, we characterized the heterogeneity of aS mobility across different temporal scales, identified the nanocluster formation, and discriminated freely diffusing and domain-constrained molecules both in and out of macro-condensates. We have also successfully investigated the effect of RNA on the aS phase transition. Strikingly, our results show that the presence of RNA drastically alters the shape and the internal mobility of aS condensates towards a solid-like state. These findings further suggest that RNA acts as a strong modifier of aS aggregation, by influencing not only the direct prion-like conversion into an amyloid state [24] but also the liquid–liquid and liquid-to-solid phase transitions of aS condensates.

Materials and methods

α-Synuclein purification and labeling

Wild-type α-synuclein (aS) and aS with the addition C141 (aS^{C141}) were respectively purified as described in [24]. Briefly, both proteins were recombinantly produced in *Escherichia coli*. The pT7-7 aS C141 plasmid was a gift from Gabriele Kaminski Schierle (Addgene plasmid #108866; RRID: Addgene_108866). After lysis with boiling, ammonium sulfate precipitation, and dialysis, the proteins were subsequently purified via anion-exchange and size-exclusion chromatography with HiTrap™Q and HiLoad™16/600 Superdex™75 columns (Cytiva, MA, USA). The cysteine in position 141 was labeled aS^{C141} with atto-488 via a maleimide reaction according to the manufacturer's instructions. Briefly, the dye is dissolved into water-free DMSO (dimethyl sulfoxide, Thermo Fisher, MA, USA) to a concentration of 10 mM. aS^{C141} dissolved in 20 mM phosphate buffer was incubated with 1.3 molar excess of atto-488-maleimide (ATTO-TEC GmbH, Germany) for 120 min at room temperature. After the incubation, the labeled protein is separated from the free atto-488 molecules via PD-10 desalting columns (Cytiva). The tagged protein was immediately checked for concentration and labeling ratio by UV–vis absorption spectroscopy (Nanodrop ND-1000, Thermo Scientific Technologies), then aliquoted, frozen, and kept at −80°C.

Glass surface passivation

μ-Slide 8-well or 18-well (Ibidi GmHb, Germany) was passivated with methyl-poly-ethylene glycol silane 5000 kDa (mPEG-silane 5K, Sigma-Aldrich, JKA3037), as shown in [46]. Briefly, multi-wells were cleaned by incubating them in 100% ethanol (Sigma–Aldrich) for 15 min, and then sonicated for 10 min. After rinsing with ultra-pure water, multi-wells were incubated in 2% (v/v) Alconox detergent (Sigma–Aldrich) in ultra-pure water for 2 h. Finally, μ-Slide 8-well were incubated in 1 g/l mPEG-silane 5K in 96 % ethanol and 0.02% (v/v) hydrochloric acid (Sigma–Aldrich) overnight, in agitation. After rinsing sequentially in ethanol and ultra-pure water, multi-wells were incubated in 1% (v/v) Tween-20 (Sigma–Aldrich) in T50 buffer (10 mM Tris–HCl, 20 mM NaCl, pH 8) for 10 min, then rinsed in T50 buffer and ultra-pure water. Multi-wells were dried using nitrogen gas flow and stored at +4°C for a maximum of 1 week.

In vitro liquid–liquid phase separation assay

The LLPS assay was performed by diluting 50 μM full-length aS and 2.5 μM (labeling ratio: 1:20) aS C141 atto-488-maleimide into the LLPS buffer [20% (wt/vol) polyethylene glycol 8000 kDa (PEG 8K, Sigma–Aldrich, Germany), 20 mM phosphate buffer (PB), 100 mM KCl, and 5 mM $MgCl_2$ (Sigma–Aldrich)]. Only for *in vitro* phase separation assay of RNA or aS-RNA, dry powder of total yeast RNA (yRNA, Roche) was dissolved in 20 mM PB. After determining the concentration of the total yRNA mixture by UV–vis absorption spectroscopy (NanoDrop Microvolume Spectrophotometer, ThermoFisher Scientific), it was added to the LLPS buffer supplemented or not with aS. For the phase separation assay of RNA-only or aS-RNA, total yeast RNA was labeled with 200 nM SYTO™13 or SYTO™85 nucleic acid stain (ThermoFisher Scientific). The sample was immediately poured onto a previously passivated μ-Slide 8-well or 18-well (Ibidi GmHb, Germany) and imaged. All measurements were performed at room temperature.

Optical microscopy experiments

Confocal microscopy imaging

Fluorescence confocal images were acquired with a Leica SP5 (Leica Microsystems, Mannheim, Germany) inverted laser scanning microscope. Atto488/SYTO™13 and SYTO™85 were excited at 488 and 570 nm, respectively. We performed the experiments with a Leica 100× APO objective lens, NA = 1.40, oil dipping. We detected the fluorescence through a Leica HyD detector in the spectral region 510–550 nm and 580–620 nm, respectively for atto488/SYTO™13 and SYTO™85. Atto488 and SYTO™85 signals were acquired sequentially to avoid any cross-talk artifact. Phase contrast images and fluorescence confocal images in Fig. 4B were acquired with a Nikon TiE inverted confocal microscope equipped with three excitation lasers (405, 488, and 561 nm) and three alkaline photomultiplier tubes. We performed the experiment with a Nikon 100× APO objective, NA = 1.25, oil dipping. Atto488 was excited at 488 nm. The 488 nm laser was a CW diode semiconductor laser (Coherent).

Image analysis

The shape and circularity [defined as $4\pi(\text{area}/\text{perimeter}^2)$] analysis was performed with Fiji software as described in [47].

Fluorescence fluctuation spectroscopy

All the fluorescence fluctuation-based experiments have been performed on a custom laser-scanning microscope designed for photon-resolved microscopy with a SPAD array detector described in detail in [37, 38, 40, 48]. The microscope uses a 5×5 SPAD array detector fabricated with a 0.16 μm BCD technology [36] and cooled to −15°C, resulting in a reduced background [48]. Briefly, the microscope excites the sample with a triggerable 485 nm pulsed laser diode (LDH-D-C-485, PicoQuant, Berlin, Germany). We coupled the laser beam into a polarization-maintaining fiber before sending it to the microscope. The laser is controlled by a laser driver, which can be synchronized via an oscillator module (PDL 828-L "SEPIA II," Picoquant). The oscillator provides also the synchronization signal to feed into the time-tagging module to measure the photon-arrival times. The excitation beam is deflected by a pair of Galvo mirrors and focused on the sample using a 100×/1.4 numerical aperture objective lens (Leica Microsystems, Wetzlar, Germany). The fluorescence signal is collected by the same objective lens, de-scanned by the two Galvo mirrors, and focused on the SPAD array detector. The measurements of monomeric aS have been acquired with the same optical system but using a single-element SPAD detector (PDM-050-CTC-FC, Micro Photon Devices, Bolzano, Italy) instead of the SPAD array detector.

Control and data-acquisition system for photon-resolved microscopy

The microscope is controlled by the BrightEyes microscope control suite (BrightEyes-MCS) [49], which operates through an FPGA-based data acquisition board (NI FPGA USB-7856R, National Instruments). The BrightEyes-MCS drives the galvo mirrors and the axial piezo stage. It also records the signals collected by the SPAD array detector, all synchronized with the scanning beam system. The core of the software, built on LabVIEW (National Instruments), is an upgrade of the original Carma application [50]. It also provides a graphical user interface for choosing the acquisition parameters and visualizing recorded signals in real-time. When fluorescence lifetime measurements are combined with imaging or spectroscopy, we integrate the BrightEyes-TTM module [38] between the SPAD array detector and the FPGA-based control unit, as described in [38]. In this setup, the BrightEyes-MCS also supplies the synchronization signals for the scanning process (i.e., pixel clock, line clock, and frame clock) to the BrightEyes-TTM. The BrightEyes-TTM also receives synchronization signals from the pulsed laser to measure photon arrival times relative to the fluorophore excitation event.

Fluorescence correlation calculation and analysis

We calculated the correlations directly on the lists of absolute photon times [51]. For spot-variation analysis, the photon lists from different subsets of SPAD array elements (chosen to mimic increasing detection volumes) were merged, and correlations were calculated for each observation volume. The temporal data was split into chunks of 5 or 10 s, and for each chunk, the correlations were calculated. The individual correlation curves were visually inspected, and all curves without artifacts were averaged. For both single-point and circular scanning [52] FCS, the correlation curves were fitted with a one- or two-component model, depending on the sample, assuming a Gaussian detection volume, as described in [48]. A detailed description of the fitting functions can be found in the Supplementary Information SA. For measurements with fluorescent beads, a one diffusing component model was used; for aS measurements, typically, a two diffusing components model was necessary (it is stated in the manuscript when another model is used). When the two-component model was used, we approximated the components to have the same brightness, as the low labeling ratio used (∼1.4%) prevented us from seeing many fluorescent labels per cluster. We kept a low aS labeling ratio to not interfere with the phase separation process of aS [53, 54]. The goodness of the fit was always checked by evaluating the reduced chi-squared and the Bayesian information criterion. For all FCS measurements acquired with the SPAD array detector, the correlation curves shown in the manuscript are related to the sum of the 25 SPAD channels (i.e., the largest detection volume). For the circular FCS measurements [52], the periodicity and radius of the scan movement were kept fixed while the autocorrelation amplitude, diffusion time, and focal spot size were fitted. This procedure was used for the fluorescent beads and allowed the different focal spot sizes to be calibrated. For the conventional FCS measurements, the focal spot size was fixed at the values found with circular scanning FCS, and the amplitude and diffusion times were fitted. The diffusion coefficient D can be calculated from the diffusion time τ_D and the focal spot size ω_0 via $D = \omega_0^2/(4\tau_D)$. For the fluorescence lifetime measurements, we measured the instrument response function of the complete setup (microscope, detector, and BrightEyes-TTM) using a solution of atto-495 (fluorescence lifetime in $H_2O = 1$ ns).

Detection volumes calibration

The detection volumes of the SPAD array detector were calibrated by circular scanning FCS [48]. Specifically, we measure the diffusion times of a sample of FluoroSpheres (YG, REF F8787, 2% solids, 20 nm diameter, actual size 27 nm, exc./em. 505/515 nm, Invitrogen, Thermo Fisher, Waltham, MA, USA) diluted in ultrapure water 1 to 5000 and drop-casted on top of a glass coverslip. The fluorescence intensity was acquired for ∼120 s and analyzed offline. All measurements were performed at room temperature. The detection volumes ω_0 are 350, 370, 404, and 420 nm for the SPAD array detector, respectively, from the smallest to the largest ω_0, Supplementary Fig. S1, and 338 nm for the single-point SPAD.

Statistical analysis

Statistical analysis was performed through OriginLab software, Version 2020 (OriginLab Corporation, Northampton, MA, USA). For each dataset, we performed a Shapiro–Wilk test to check the normality of the data distribution. When the hypothesis of normality was rejected, a non-parametric test (Mann–Whitney or Kruskal–Wallis tests) followed by a post hoc test (Dunn's or Conover's tests) was performed. When the hypothesis of normality was accepted, an ANOVA one-way parametric test followed by a Tukey's test was performed. The exact P-values are reported in Supplementary Table S1.

Results

In vitro reconstitution of α-synuclein phase separation

We first characterized the diffusivity of purified full-length aS via FCS in phosphate buffer (PB), under non-LLPS-inducing conditions (Fig. 2A, top). A one-diffusing component model was sufficient to fit the FCS autocorrelation data, hinting at a uniform, noninteracting population of freely diffusing molecules (Supplementary Fig. S2). The retrieved diffusion coefficient, $D_{\mathrm{app}} = 134 \pm 4\ \mu\mathrm{m}^2/\mathrm{s}$, and its related hydrodynamic radius, $r_H = 1.65 \pm 0.05$ nm (calculated with the Stokes–Einstein formalism), are both compatible with literature values for monomeric aS [53, 55–57].

Regarding the aS LLPS assay, the protein has been reported to undergo LLPS at concentrations ranging from 5 to 500 μM upon different concentrations of the molecular crowder polyethylene glycol (PEG-8000, henceforth referred to as PEG). Only at high concentrations (500 μM), spontaneous LLPS occurs in the absence of a crowder [12]. These extremely high concentrations are far from endogenous levels, making them biologically less relevant. Therefore, we performed all LLPS measurements at an aS concentration of 50 μM, which approximates its reported concentration in synapses [58]. At 50 μM, LLPS was observed only in the presence of PEG, which acts to reduce the energy barrier for phase separation [12]. For PEG to function as a suitable molecular crowder, it should promote aS LLPS by lowering the threshold concentration required for phase separation while not inducing phase separation in biomolecules that do not inherently undergo this process. To assess the suitability of a 20% PEG buffer (20% PEG in 20 mM PB) for LLPS, we used GFP as a negative control [59]. GFP is a stably folded protein that lacks intrinsic phase-separating properties and is expected to remain homogeneously distributed in solution without forming condensates or aggregates. As expected, confocal microscopy images of GFP in 20% PEG buffer confirmed a homogeneous distribution of the protein (Supplementary Fig. S3A).

Next, we measured the effect of PEG on aS LLPS at two different concentrations (10% and 20%). In the presence of 10% PEG, the protein at the concentration of 50 μM has been reported not to undergo immediate and spontaneous macroscopic phase separation, while at the higher concentrations (20% PEG) it is supposed to form micrometer-sized, optically resolvable liquid-like condensates [27]. As expected, confocal images do not reveal the formation of a visible, macroscopic dense phase at 10% PEG (Supplementary Fig. S3B). Although macroscopic phase separation does not occur, FCS measurements detect multiple diffusing components. This may suggest that small, diffraction-limited condensates or nanoscale assemblies may be present, even under sub-saturation conditions. Specifically, upon the addition of PEG, the autocorrelation function $G(\tau)$ could not be described anymore by a one-diffusing component model (Supplementary Fig. S5A). By employing a two-diffusing component model, we detected the presence of a fast diffusing component with $D_{\mathrm{app}} = 66 \pm 4\ \mu\mathrm{m}^2/\mathrm{s}$ and a slow diffusing one with $D_{\mathrm{app}} = 0.66 \pm 0.19\ \mu\mathrm{m}^2/\mathrm{s}$ (Supplementary Fig. S5A).

Further increasing the concentration of PEG to 20% triggers macroscopic LLPS, which is confirmed by the formation of spherical, micron-sized condensates (Fig. 2A, middle and bottom). To characterize the diffusivity of aS at the nanoscale, we performed FCS measurements in the dilute and dense phases (Fig. 2B; Supplementary Fig. S5B and C). Compared to the dilute phase, the autocorrelation curve $G(\tau)$ of the dense phase shows a smaller amplitude $G(0)$ and a shift towards longer time delays. The amplitude of the autocorrelation curve is inherently linked to the average number of molecules within the observation volume, confirming a higher concentration of molecules in the dense phase (Supplementary Information). The observed shift of $G(\tau)$ of the dense phase toward longer time delays suggests slower diffusivity compared to the dilute phase, potentially indicative of protein oligomerization or increased viscosity (Fig. 2B–G). Notably, the characteristic diffusion time τ_D of the autocorrelation curve (the time at which the correlation amplitude halves) is directly related to the diffusion coefficient and, consequently, the diffusivity of the sample. A longer τ_D suggests slower diffusivity, whereas a shorter τ_D indicates faster molecular motion.

As for 10% PEG, two distinct diffusing components are detected in the FCS curves for both phases (Supplementary Fig. S5B and C). To characterize them further, we analyzed their diffusion modes by performing svFCS. If the diffusing species moves with Brownian motion, the diffusion time will decrease or increase correspondingly as the observation area changes. If the diffusion time τ_D does not scale proportionally with the observation area ω_0^2, the type of movement in the sample is no longer described by free diffusion. By plotting the diffusion law τ_D) (the diffusion time versus the observation area), we can evaluate the type of movement with linear regression: if the intercept of the linear regression τ_D is 0, molecules are freely diffusing; if negative, molecules are highly restricted in mobility (such as inside the dense meshwork of the cytoskeleton); if positive, molecules are moving in a domain-confined sample (Fig. 1) [35]. In the latter, the intercept value is directly proportional to the confinement strength, which reflects the energy barrier needed for the molecules to exit the micro-domain [60].

The svFCS analysis revealed a free diffusion mode for the fast diffusing component ($\tau_D(0) = 0.003 \pm 0.214\,ms$ for the dilute phase, $\tau_D(0) = 0.4 \pm 1.4\,ms$ for the dense phase, Fig. 2D). We hypothesized that the fast component refers to monomeric aS, freely diffusing in both dilute and dense phases. To validate our hypothesis, we analyzed the τ_D distribution for the fast diffusing component in both phases (Fig. 2C). Overall, the diffusion time τ_D can be influenced by changes in viscosity and/or hydrodynamic radius (Supplementary Information). Assuming that the viscosity of the dilute phase (20% PEG buffer) is constant over time, τ_D is mainly affected by changes in the hydrodynamic radius and, ultimately, in the mono- or oligomeric state of aS. To estimate τ_D of the monomeric aS in LLPS buffer (20% PEG), we measured the one of GFP in both PB and LLPS buffer (Supplementary Fig. S4). Since it does not phase separate or oligomerize, GFP is commonly used to study changes in viscosity in phase separation buffers [61]. Thereby, potential changes in the GFP diffusion time between PB and LLPS buffers are exclusively due to a difference in the buffer viscosity (Supplementary Fig. S3A). Comparing τ_D of GFP measured in both buffers, we retrieved the viscosity of the 20% PEG buffer and, ultimately, the expected τ_D of monomeric aS for the same buffer ($\tau_D = 2.13 \pm 0.07\,ms$, Supplementary Fig. S4). The median of the τ_D distribution of the dilute phase ($\tau_D = 1.80$ ms, Fig. 2C) corresponds well to the τ_D associated with the monomeric protein, confirming that aS is mainly organized in a freely diffusing monomeric state within the dilute phase. On the other hand, the heterogeneous τ_D distribution of the dense phase reflects a more complex micro-environment (Fig. 2C). Comparing the percentage of the fast diffusing component for both phases, we measured a higher percentage of the aS fast component for the dilute phase, hinting again at a more complex micro-environment inside the condensates (Fig. 2F).

Regarding the slow diffusing component, svFCS revealed non-Brownian motion for the dense and dilute phases, as, in both, the intercept of the linear regression of the diffusion law $\tau(\omega_0^2)$ is not zero ($\tau_D(0) = 81 \pm 22\,ms$ for the dilute phase, $\tau_D(0) = 60 \pm 25$ ms for the dense phase, Fig. 2E). Regarding the non-Brownian component present in the dilute phase, several studies have shown that crowded environments, such as those mimicked by PEG, can induce anomalous diffusion of proteins or molecular complexes that would otherwise freely diffuse in solution [62]. This phenomenon is generally attributed to factors such as the temporary, dynamic mesh-like network formed by PEG molecules, excluded volume effects, or the combination of these elements. Interestingly, anomalous diffusion becomes more pronounced as the size of the molec-

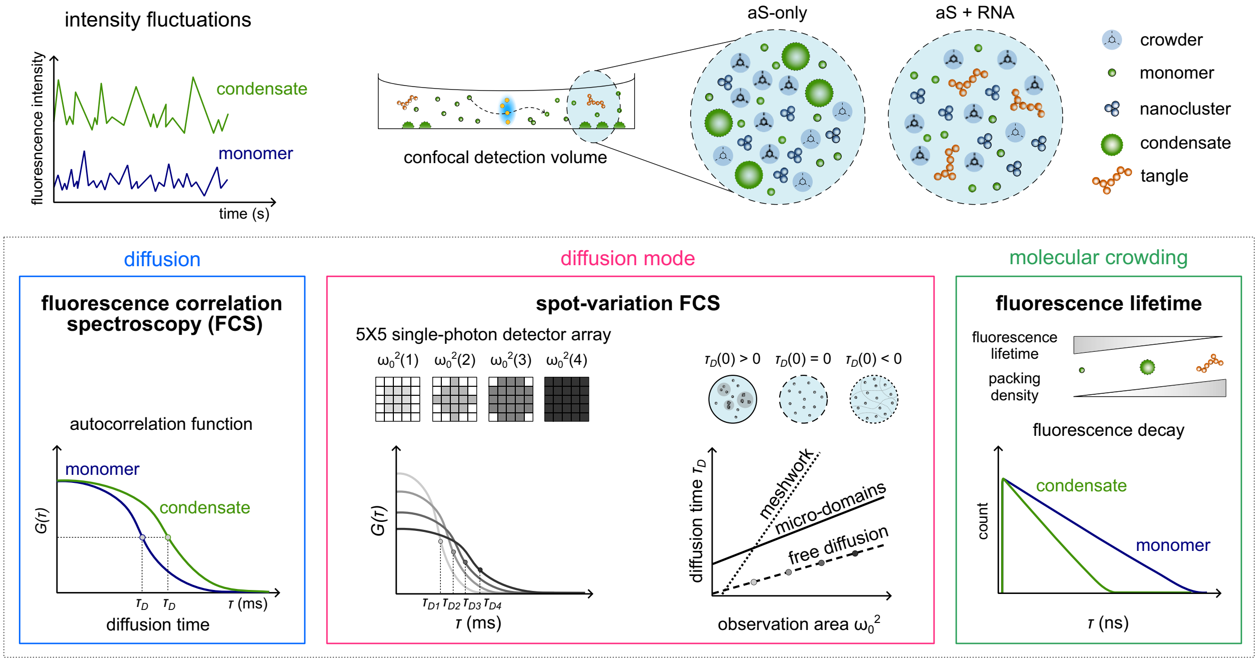

Figure 1. Schematic representation of the experimental and analysis session. The phase separation assay is a mixture of aS, aS-atto488, and, in the case of the RNA experiment, total yeast RNA. The sample is placed into a closed chamber and under a confocal laser scanning microscope equipped with a 5 × 5 single-photon array detector. Fluorescence over time is acquired in different sample positions. The same dataset of fluorescence over time can be used to perform fluorescence lifetime quantification or FCS-based methods (FCS and spot-variation FCS).

ular complex increases [63]. This explains why only the slow-diffusing component of the dilute phase, rather than the fast component, is affected. In addition to the crowder effect, nanoclusters may interact with aS molecules in the surrounding solution or with other clusters, especially in scenarios where they act as precursors to macro-condensates. These interactions can further explain or contribute to deviations from the free diffusion behavior.

Apart from the non-Brownian diffusion, the slow-diffusing component in the dilute phase exhibits D_{app} of $0.60 \pm 0.08\ \mu\text{m}^2/\text{s}$, corresponding to clusters with $r_{\text{H}} = 69 \pm 12$ nm. Mass photometric studies on aS phase-separated systems already proposed the presence of diffraction-limited assemblies, referred to as nanoclusters, under the same conditions (50 μM aS in 20% PEG buffer) [27]. Along with the nanoscale size, the slow-diffusing component in the dilute phase has all the properties attributed to nanoclusters: (i) the formation is immediate and spontaneous; (ii) the assembly also occurs upon sub-saturated concentrations, where no instantaneous macroscopic LLPS is triggered (10% PEG buffer) [27]. All these observations allow us to associate the slow diffusing component in the dilute phase with nanoclusters. Notably, at subsaturated conditions (10% PEG), nanoclusters are larger than the ones in 20% PEG buffer ($r_{\text{H}} = 93 \pm 9$ nm for 10% PEG).

While the non-Brownian motion of nanoclusters can be attributed to obstacles in the surrounding solution (e.g. PEG-induced crowding, nanocluster fusion), the domain-confined diffusion of aS in the dense phase arises from a different mechanism. In the dense phase, FCS measurements of aS were performed in internal regions of non-moving macro-condensates. The non-Brownian diffusion observed for aS within these condensates reflects their heterogeneous internal structure, with certain micro-domains where aS diffusion is restricted. For the dense phase, we speculate that domain-confined aS reflects the portion of aS forming weak intermolecular interactions, which are essential for condensate formation. In contrast, the freely diffusing portion is the one readily exchanged with the external environment.

RNA does not affect the α-synuclein dilute phase

Once we had characterized the diffusivity of aS under LLPS conditions, we studied the potential effect of RNA on the same *in vitro* system. In this work, we used total yeast RNA (henceforth referred to as RNA), which is known to undergo phase transitions in a PEG-based buffer. Depending on the concentration and the molecular weight of PEG, total RNA undergoes phase separation, forming either liquid-like, round-shaped condensates or irregular-shaped structures (tangles) [64]. To confirm the behavior of RNA in LLPS buffer (20% PEG), we tested three different concentrations of RNA (5, 50, and 500 ng/μl) labeled with SYTO™13 under the same LLPS conditions used for aS. By confocal imaging, we confirm the spontaneous formation of spherical condensates at all RNA concentrations (Fig. 3A, first column).

Next, aS and RNA were combined, and phase separation was triggered in the LLPS buffer. When aS LLPS is induced in the presence of RNA, the dense phase shows an irregular shape rather than the spherical one obtained for RNA- or protein-only condensates (Figs 2A and 3A, and Supplementary Fig. S3C). In the presence of RNA, aS forms smaller droplets attached in a longer chain, a sign that the coalescence into larger condensates is impaired [65]. Similar structures, or tangles, have been already observed in RNA-only conditions upon high salt concentrations [64].

Liquid-like condensates commonly exhibit a spherical shape due to surface tension, while aggregated aS is packed in irregular-shaped and fibrillar structures. For this rea-

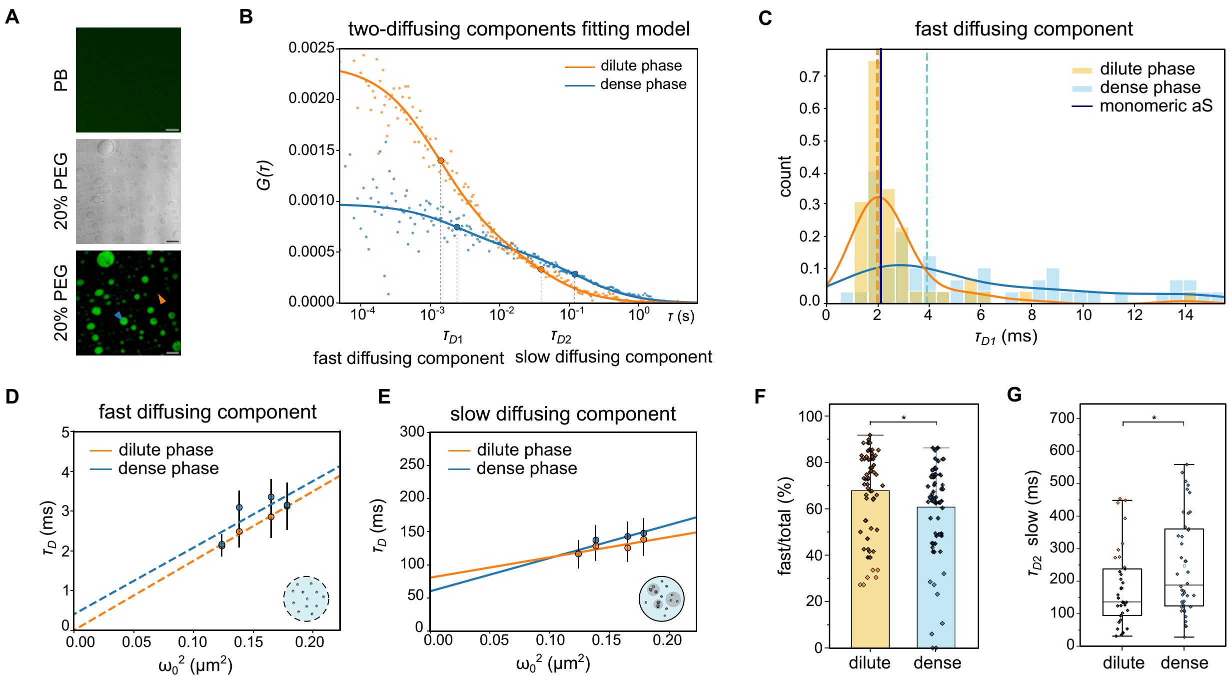

Figure 2. aS forms nano- and micro-complexes in a phase-separated system. (**A**) Confocal image (top) of 700 nM monomeric aS-atto488 in PB. Phase contrast microscopy image (middle) and confocal (bottom) image of aS in LLPS buffer. In the presence of 20% PEG, aS spontaneously forms a dense phase surrounded by a dilute phase. Scale bars: 5 μm. (**B**) Representative autocorrelation functions in the dilute and the dense phases of aS, as indicated by the arrows in panel (A). The lines represent the fit of the autocorrelation curves with a two-component fitting model. Diffusion times for the fast (τ_{D1}) and slow (τ_{D2}) diffusing components are shown. (**C**) Histogram of diffusion times τ_{D1} measured for the fast diffusing component in the dense and dilute phases. The solid lines represent the upper envelope of the histograms. The dashed lines represent the median of both distributions; the vertical solid line indicates the median of the τ_D for monomeric aS in the LLPS buffer. $n = 50$ (dilute phase), 53 (dense phase). (**D** and **E**) svFCS analysis of the fast (D) and slow (E) diffusing components for both dilute and dense phases. Diffusion times are plotted against the observation areas $\omega_0{}^2$ to retrieve the diffusion law $\tau_D(\omega_0{}^2)$ (dashed line). Data points and error bars are, respectively, mean and standard deviations of multiple measurements ($n = 4$ independent experiments). (**F**) Percentage of the fast diffusing component in the dilute and the dense phases. $n = 40$ (dilute phase), 48 (dense phase). Mann–Whitney statistical test (*: P-value < 0.05). (**G**) Box-plot of diffusion times τ_{D2} measured for the slow diffusing component in the dilute and the dense phase. $n = 37$ (dilute phase), 42 (dense phase). Mann–Whitney statistical test (*: P-value < 0.05). The horizontal line in each box represents the median, the edges are the 25th and 75th percentile, and the vertical line extends to the minimum and maximum data points.

son, circularity is an ideal parameter for discriminating between liquid-like and solid-like condensates [66–68]. We analyzed several confocal images to quantify the circularity [4π(area/perimeter^2)] of condensates in the presence or absence of total RNA (Supplementary Fig. S8A). We observed a strong reduction of the parameter (1 indicates a perfect sphere, 0 indicates a more elongated shape) upon adding RNA (Supplementary Fig. S8B). The loss in the circularity and the structural transition towards an irregular shape suggests that aS, in the presence of total RNA, phase separates into tangles. Interestingly, these structures were never observed for the aS-only condensates. Moreover, no visible concentration-dependent effect regarding the size and number of tangles can be appreciated by confocal images (Fig. 3A). The RNA staining with the nucleic acid dye SYTO™85 revealed the colocalization of RNA with the protein, confirming the actual recruitment of the nucleic acid within the aS dense phase (Fig. 3A).

We performed svFCS in both dilute and dense phases to explore the effect of RNA on aS LLPS at the nanoscale. As an initial step, we ruled out any potential changes in the viscosity of the LLPS buffer caused by the addition of RNA, as this could affect τ_D and thus future considerations regarding the molecular organization of aS in the dilute phase (Supplementary Fig. S6). Measurements were acquired at all three previously tested RNA concentrations to assess any potential concentration-dependent effects on molecular mobility. As for the protein-only LLPS system, conventional FCS measurements within the dilute phase revealed the presence of two diffusing components (Supplementary Fig. S7A–C). Regarding the fast diffusing component in the dilute phase, svFCS analysis indicated that aS freely diffuses in the sample ($\tau_D(0) = 0.52 \pm 0.30, 1.01 \pm 0.25, 0.68 \pm 0.18\, ms$, respectively for 5, 50, and 500 ng/μl RNA, Fig. 3B). The distribution of the diffusion times τ_D associated with the fast component shows that the freely diffusing protein within the dilute phase is mainly monomeric. Additionally, the median of the distributions is comparable with the one measured for aS-only dilute phase (Fig. 3D for 500 ng/μl RNA, Supplementary Fig. S7D for 5 and 50 ng/μl RNA). Possibly, this component represents the monomeric aS not participating in the condensate formation. Surprisingly, while no differences are seen in the dilute phase in terms of diffusivity when RNA is present, the average percentage of aS monomers (fast diffusing component) is higher at low RNA concentrations (5 and 50 ng/μl). This effect disappears when RNA concentration increases up to 500 ng/μl. Indeed, at the highest tested RNA concentration, the aS diffusivity does not change compared to the protein-only condition (Fig. 3E).

The slow diffusing component in the dilute phase exhibits micro-domain confinement as diffusion mode across all tested RNA concentrations ($\tau_D(0) = 103 \pm 23, 110 \pm$

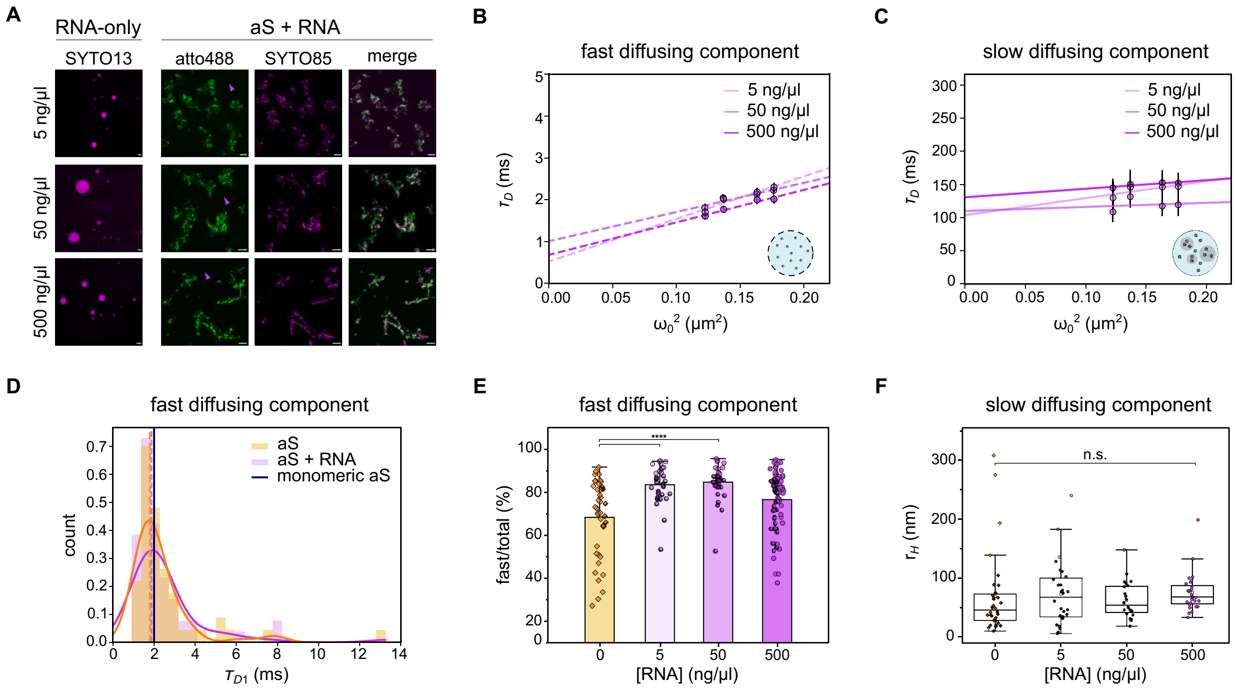

Figure 3. Effect of total yeast RNA on aS phase-separated system. (**A**) On the left, confocal images of 5, 50, and 500 ng/μl RNA in LLPS buffer. On the right, confocal images of aS, aS-atto488 and RNA at different concentrations of RNA. A merge of both channels is shown on the right. Scale bars: 5 μm. (**B** and **C**) svFCS analysis of the fast (B) and slow (C) diffusing components of aS in the presence of RNA within the dilute phase. Diffusion times τ_D are plotted against the observation areas $\omega_0{}^2$. Data points and error bars are, respectively, mean and standard deviations of multiple measurements ($n = 4$ independent experiments). (**D**) Histogram of diffusion times τ_D for the fast diffusing component of aS in the dilute phase under LLPS condition alone and in the presence of RNA (500 ng/μl). The solid lines on top of the histograms represent the upper envelope of the histogram. The dashed lines represent the medians of both distributions (1.88 ms for RNA); the vertical solid line indicates the median of the τ_D measured for the monomeric aS. $n =$ 50 (aS), 57 (aS + RNA). (**E**) Percentage of the fast diffusing component in the dilute phase of aS in the presence of RNA. From left to right, $n = 40$, 30, 31, 77. Kruskal–Wallis statistical test followed by Dunn's test (**** P-value < 0.00005). (**F**) Box plots of the hydrodynamic radius (r_H) in the dilute phase of aS alone and in the presence of RNA. No significant difference is appreciated among all conditions. From left to right, $n = 38$, 39, 41, and 56. Kruskal–Wallis statistical test (n.s.: P-value > 0.05).

40, $130 \pm 8\,ms$ for 5, 50, and 500 ng/μl RNA, respectively, Fig. 3C). Apart from anomalously diffusing , this component represents nanometer-sized aS clusters ($r_H = 71 \pm 10, 62 \pm 9$, and 75 ± 6 nm for 5, 50, and 500 ng/μl RNA, respectively, Fig. 3F). The aS slow-diffusing component exhibits all the features previously attributed to nanoclusters, and its detection provides evidence that nanocluster formation occurs even in the presence of RNA. No significant differences in the confinement strength $\tau_D(0)$ are observed across the three RNA concentrations (Fig. 3C). Despite no significative changes in size upon RNA addition (Fig. 3F), we observed an increase in the confinement strength of nanoclusters from the aS-only to the aS+RNA condition. We speculate that RNA may induce a more heterogeneous surrounding medium or promote transient interactions at the nanocluster surface, thereby further constraining their mobility.

RNA alters material properties of α-synuclein dense phase

Fibrillar structures similar to the ones obtained for aS and RNA were already observed for the phase separation of RNA-binding proteins in the presence of RNA and were associated with a less dynamic state [65]. However, while the irregular shape of these tangles suggests a solid-like nature, neither confocal imaging nor svFCS can offer insights into the dense phase of aS when RNA is present. Specifically, FCS measurements show no correlation in any RNA condition. We speculate that the absence of correlation among fluorescence fluctuations stems from reduced liquid-like properties inside the tangles. The highly constrained environment of aS molecules within solid-like condensates hints toward the presence of a substantial immobile fraction, which makes FCS an unsuitable method to study diffusivity. The presence of a significant immobile fraction and the irregular shape of the dense phase further support the hypothesis that RNA actively contributes to the transition towards solid-like aS condensates. For this reason, alternative approaches beyond FCS and related methods should be considered.

As a sensor of the molecular environment, fluorescence lifetime is a promising alternative for probing the different material properties of biomolecular complexes. Certain dyes exhibit changes in fluorescence lifetime in response to a variety of physical parameters, including quenching, molecular crowding, viscosity, pH, and ion composition [43, 69, 70]. The effect on the fluorescence lifetime trend, whether shorter or longer, is highly dependent on the intrinsic properties of the fluorophore and the underlying mechanisms. From an instrumental point of view, the SPAD array detector combined with the time-tagged detection allows the analysis of the photon-resolved dataset at both the micro-second scale requested by FCS and the sub-nanosecond scale requested by fluorescence

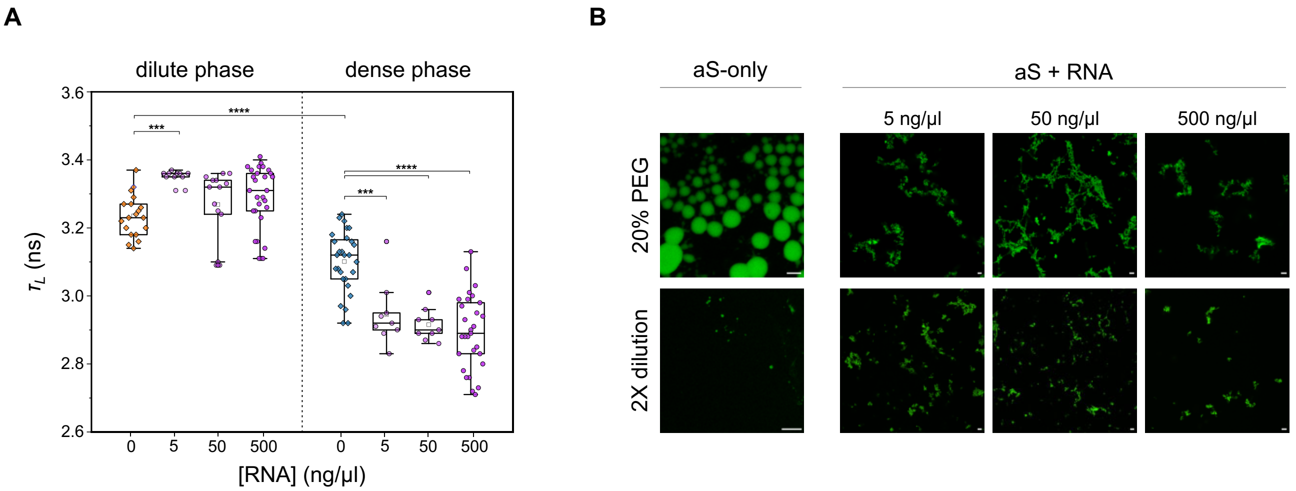

Figure 4. Fluorescence lifetime as a sensor for the condensation degree of aS in a phase-separated system. (**A**) Box plots of the fluorescence lifetime (τ_L) of aS-atto488 in the dilute (left) and dense (right) phase at different RNA concentrations. From left to right, $n = 19$, 10, 14, 29, 28, 9, 9, and 29. One-way ANOVA and Kuskal–Wallis test followed by a Dunn's test for the dilute phase (***P-value < 0.0005, ****P-value < 0.00005). (**B**) Confocal images of aS in LLPS buffer at different RNA concentrations. Top is LLPS buffer, bottom is after having diluted LLPS buffer twice with 20 mM PB.

lifetime. This allows us to correlate diffusion and fluorescence lifetime analysis on the same measurement [38, 40].

We measured the fluorescence lifetime (τ_L) of aS-atto488 both in dilute and dense phases, with and without RNA. In the dilute phase, we observed no variations in the fluorescence lifetime for all the conditions, except for the 5 ng/µl RNA condition (Fig. 4A). Interestingly, svFCS measurements revealed that the dilute phase is mainly composed of monomeric aS, with the 5 ng/µl RNA condition differing in the percentage of fast-diffusing monomers over nanoclusters. In the 5 ng/µl RNA condition, the monomer ratio is indeed higher than that observed for aS-only (Fig. 3E). For the dense phase, shorter average lifetime values were measured within condensates for all conditions when compared to the dilute phase. Surprisingly, a significative reduction in the fluorescence lifetime values is also observed between protein-only condensates and aS-RNA tangles. This observation agrees well with the scenario in which RNA actively contributes to the liquid-to-solid transition of aS. The trend in the fluorescence lifetime is independent of the RNA concentration, suggesting that RNA increases the overall condensation/aggregation propensity of the protein irrespective of its concentration (Fig. 4A).

The reduction of aS-atto488 fluorescence lifetime within condensates cannot be universally attributed to the condensation degree, as multiple factors may contribute to this effect. As liquid-like condensates mature into aged or solid-like condensates, molecules and their attached dyes are brought into closer proximity. For certain dyes, this increased molecular packing can lead to shorter τ_L values due to self-quenching [71]. While the exact mechanism underlying the changes in aS-atto488 fluorescence lifetime remains unclear, self-quenching and a higher packing density of aS molecules in condensates (compared to monomers) and tangles (compared to aS-only condensates) represent a possible explanation. In this context, the increased percentage of monomers in the 5 ng/µl RNA condition correlates well with the longer retrieved lifetime.

We acknowledge that the fluorescence lifetime alone may not be a definitive indicator of the physical state of condensates. Thereby, in addition to the morphological differences between aS condensates and tangles already discussed, we also tested the liquid-like properties by assessing the reversibility of the aS condensates under all four conditions. We diluted the 20% PEG buffer twice in PB. After 20 min upon dilution, we observed the almost complete dissolution of the aS-only condensates, while the aS–RNA tangles reduced their size but did not fully disappear (Fig. 4B). As the dilution reduces the crowding effect of the buffer (by effectively reducing the PEG concentration), if the condensates are purely liquid-like, they will dissolve; if they are partially or completely solid-like, they will not.

Discussion

Our study demonstrates the significant impact of RNA on the phase separation and aggregation of aS at the nanoscale using photon-resolved microscopy.

In the absence of RNA, we showed that aS immediately and spontaneously forms nanoclusters in the dilute phase, even below the saturation concentration required for macroscopic phase separation. This aligns with recent findings that phase separation can occur at much lower concentrations within cells than previously assumed [14]. The role and eventual maturation of nanoclusters in LLPS systems remain unknown, with some remaining independent, metastable structures, and some others coalescing into larger condensates [72]. For aS, it has been proposed that they act as precursors to macrocondensates, thus potentially having an active role in the protein phase transitions [27].

When RNA is introduced, aS still exhibits two diffusing components in the dilute phase: freely diffusing monomers and anomalously diffusing nanoclusters. Although RNA does not significantly alter the nanocluster size, it modulates the monomer/nanocluster ratio. Lower RNA concentrations reduce nanocluster prevalence, indicating a potential negative impact of RNA on nanocluster formation. Moreover, RNA enhances the confinement strength experienced by aS nanoclusters. While monomeric aS in the dilute phase likely does not interact with RNA, as suggested by the absence of diffusion changes, it remains unclear whether RNA is present within nanoclusters. However, the observed differences in confinement strength could provide a basis for possible interactions between of RNA and aS in nanoclusters, potentially affecting their diffusion mode. This nuanced role of RNA in modulating aS diffusivity suggests that the effect of RNA on aS dilute phase probably depends more on its sequence and structure rather than its concentration.

In the dense phase, RNA promotes the liquid-to-solid transition of aS, as evidenced by the reduced circularity of the dense phase and the formation of irregular, more solid-like tangles. Additionally, both the resistance to buffer dilution of aS–RNA tangles and the absence of aS fluorescence intensity fluctuations in aS–RNA condensates hint at immobile molecules and support the hypothesis of their solid-like nature. While the different morphology suggests changes at the microscale, the shorter fluorescence lifetime observed within these tangles (compared to aS-only condensates) indicates that RNA incorporation also influences aS condensates at the nanoscale. Similar behaviors have been observed for other organic dyes in phase transition studies, where a shorter fluorescence lifetime has been linked to more aged condensates [71, 73] or aggregates [42, 43, 74]. Although further investigation is needed to identify the mechanism underlying the change in aS-atto488 fluorescence lifetime, the higher degree of molecular compaction in aS–RNA condensates may provide a potential explanation for the observed fluorescence lifetime trend.

In a more general context, RNA is known to significantly impact protein aggregation, with certain RNA structures promoting or inhibiting these processes depending on their interaction with the protein [75–77]. We have previously observed that certain RNA species are relevant for LLPS, but it is also plausible that other species are crucial for the liquid-to-solid phase transition [23, 78, 79]. This distinction underscores the complexity of the role of RNA in protein aggregation and highlights the need for further research to delineate these effects.

In its monomeric form, the intrinsic flexibility of aS typically prevents stable interactions with RNA, except for RNA G-quadruplexes structures [23]. While aS is not traditionally classified as an RNA-binding protein, computational predictions indicate a potential for RNA binding [80], which becomes biologically relevant during aggregation. Under aggregation conditions, the N-terminal region of aS is exposed to the solvent and available for RNA interactions. This results in RNA acting as a molecular bridge between the N-terminus of different aS molecules, bringing them closer [24].

Condensates create a chemically diverse environment where RNA can partition due to multiple factors. RNA incorporation into condensates can be influenced by its own solubility and self-interaction properties, as well as by conformational changes of aS within the dense phase that enhance its affinity for RNA. As for aggregates, we speculate that aS adopts an RNA-binding conformation even under the conditions investigated here, promoting the formation of aS–RNA tangles. Within liquid-like condensates, the extremely high concentrations of aS [13] may induce structural changes that expose RNA-binding regions, facilitating more specific interactions, such as those with G-rich RNA, that are otherwise transient in solution. This shift from non-binding to RNA-binding states underscores the dynamic nature of aS and its functional versatility in different aggregation and, eventually, phase-separated states.

Under stress conditions, G-quadruplex RNAs, especially synaptic mRNAs, phase separate and, as a result, directly interact with the aS N-terminal region, accelerating protein aggregation and synaptic dysfunction [23]. As with many amyloidogenic proteins, aS is also predicted to interact with its cognate RNA, thus modulating its own expression and aggregation rate [80]. Even non-coding RNAs seem to have the potential to interact with aS [81]. Taking into consideration the complexity of RNA in aS phase transitions, this work employs total RNA, thus ensuring an even distribution in terms of RNA structures and compositions. Our study elucidates the role of total RNA in *in vitro* aS phase transitions and provides an initial foundation for understanding how aS exploits liquid–liquid and liquid-to-solid transitions in its physiological and pathological roles.

The presence of aS in multicomponent MLOs, such as processing bodies [18], and its *in vitro* LLPS dependence on molecular crowders, suggest that aS alone probably does not spontaneously drive LLPS like canonical phase-separating proteins (e.g., TDP43 and FUS) [82, 83]. Biomolecular condensates are indeed composed of scaffold molecules, which initiate the phase separation process, and client molecules, which are subsequently recruited into the condensate [84]. In this context, it is plausible that aS acts as a client, as has been shown for aS/Tau condensates [15]. However, the ability of aS to partition into condensates indicates that it can leverage LLPS to mediate both physiological and pathological functions. Notably, interactions with lipids and other cellular components promote the aS liquid-to-solid transition, reinforcing the hypothesis that aS acts in synergy with other biomolecules to regulate its phase transitions [25].

Finally, given the complex, multiscale nature of LLPS processes, integrating multiple quantitative methods is crucial for uncovering the underlying mechanisms. Our photon-resolved platform represents a powerful tool for studying protein phase transitions [40]. Furthermore, as this framework is compatible with living cells, it is also suitable for studying aS LLPS in more complex environments where it is physiologically coupled with RNA. This understanding could ultimately facilitate the development of therapeutic strategies targeting the early stages of protein aggregation in neurodegenerative diseases.

Acknowledgements

We thank all members of the Molecular Microscopy and Spectroscopy group and the RNA Systems Biology group at the Istituto Italiano di Tecnologia (IIT); Simone Civita and Matteo Mariangeli (Nanoscopy & NIC@IIT, IIT) for valuable discussions; Dr. Michele Oneto and Dr. Marco Scotto (Nikon Imaging Center, IIT) for support on the experiments; Prof. Alberto Tosi, Prof. Federica Villa, Dr. Mauro Buttafava (Politecnico di Milano), Dr. Marco Castello, and Dr. Simonluca Piazza (Genoa Instruments) for the realization of the single-photon-avalanche-diode detector array; all members of the RNA Initiative at the Istituto Italiano di Tecnologia, Prof. Stefano Gustincich (non-coding RNAs and RNA-based therapeutics, IIT) and Dr. Francesco Nicassio (Genomics Science, IIT) for their contribution to the long-term vision of this project.

Author contributions: G.V. and S.Z. conceptualized the study. E.P., E.S., and G.V. developed the methodology. E.S. designed the software and resources, and both E.S. and E.P. performed data curation. Formal analysis was conducted by E.P. and S.Z. The investigation was carried out by S.Z.

and J.R., who prepared the protein samples, with S.Z. conducting the experiments. E.Z., G.G.T., E.P., and G.V. supervised the project. G.V. also managed project administration. S.Z., E.P., and J.R. wrote the original draft of the manuscript, and all authors contributed to reviewing and editing the final version.

Supplementary data

Supplementary data is available at NAR Molecular Medicine online.

Conflict of interest

G.V. has a personal financial interest (co-founder) in Genoa Instruments, Italy.

Funding

This project has received funding from: the Compagnia San Paolo, "Augmented fluorescence correlation spectroscopy with a novel SPAD array detector to observe complex biological processes in living cells," Trapezio No.71100 (E.P.); the European Research Council, "BrightEyes," ERC-CoG No. 818699 (G.V.), "ASTRA," ERC-SyG No. 855923 (G.G.T.); the European Innovation Council, "ivBM-4PAP," Pathfinder No. 101098989 (G.G.T.); the NextGeneration EU PNRR MUR - M4C2 - Action 1.4 - Call 'Potenziamento strutture di ricerca e creazione di 'campioni nazionali di R&S' (CUP J33C22001130001), "National Center for Gene Therapy and Drugs based on RNA Technology„" No. CN00000041 (S.Z, G.G.T., and G.V.).

Data availability

All the codes used for analyzing the photon time-tagging measurements (fluorescence lifetime fluctuation spectroscopy) have been deposited in the GitHub BrightEyes-TTM repository as a part of a larger open-hardware/software project that aims at democratizing single-photon laser-scanning microscopy based on SPAD array detector [38], and it is available also on Zenodo (https://doi.org/10.5281/zenodo.7064910) [85]. All the data, images, and file measurements used for the manuscript have been deposited on the IIT Dataverse repository (https://doi.org/10.48557/SFXH9V).

References

1. Chiti F, Dobson CM. Protein misfolding, functional amyloid, and human disease. *Annu Rev Biochem* 2006;**75**:333–66. https://doi.org/10.1146/annurev.biochem.75.101304.123901
2. Buell AK, Galvagnion C, Gaspar R *et al.* Solution conditions determine the relative importance of nucleation and growth processes in alpha-synuclein aggregation. *Proc Natl Acad Sci* 2014;**111**:7671–6. https://doi.org/10.1073/pnas.1315346111
3. Meisl G, Michaels TCT, Arosio P *et al. Dynamics and Control of Peptide Self-Assembly and Aggregation*. Singapore: Springer, 2019, 1–33. https://doi.org/10.1007/978-981-13-9791-2_1
4. Louros N, Schymkowitz J, Rousseau F. Mechanisms and pathology of protein misfolding and aggregation. *Nat Rev Mol Cell Biol* 2023;**24**:912–33. https://doi.org/10.1038/s41580-023-00647-2
5. Alberti S, Hyman AA. Biomolecular condensates at the nexus of cellular stress, protein aggregation disease and ageing. *Nat Rev Mol Cell Biol* 2021;**22**:196–213. https://doi.org/10.1038/s41580-020-00326-6
6. Shin Y, Brangwynne CP. Liquid phase condensation in cell physiology and disease. *Science* 2017;**357**:6357. https://doi.org/10.1126/science.aaf4382
7. Lashuel HA, Overk CR, Oueslati A *et al.* The many faces of alpha-synuclein: from structure and toxicity to therapeutic target. *Nat Rev Neurosci* 2012;**14**:38–48. https://doi.org/10.1038/nrn3406
8. Burré J, Sharma M, Tsetsenis T *et al.* Alpha-synuclein promotes SNARE-complex assembly *in vivo* and *in vitro*. *Science* 2010;**329**:1663–7. https://doi.org/10.1126/science.1195227
9. Schaser AJ, Osterberg VR, Dent SE *et al.* Alpha-synuclein is a DNA binding protein that modulates DNA repair with implications for Lewy body disorders. *Sci Rep* 2019;**9**:10919. https://doi.org/10.1038/s41598-019-47227-z
10. Goedert M, Jakes R, Spillantini MG. The synucleinopathies: twenty years on. *J Parkinsons Dis* 2017;7:S51–69.
11. Iljina M, Garcia GA, Horrocks MH *et al.* Kinetic model of the aggregation of alpha-synuclein provides insights into prion-like spreading. *Proc Natl Acad Sci* 2016;**113**:1206–15. https://doi.org/10.1073/pnas.1524128113
12. Ray S, Singh N, Kumar R *et al.* Alpha-Synuclein aggregation nucleates through liquid–liquid phase separation. *Nat Chem* 2020;**12**:705–16. https://doi.org/10.1038/s41557-020-0465-9
13. Dada ST, Hardenberg MC, Toprakcioglu Z *et al.* Spontaneous nucleation and fast aggregate-dependent proliferation of Alpha-synuclein aggregates within liquid condensates at neutral pH. *Proc Natl Acad Sci USA* 2023;**120**:9. https://doi.org/10.1073/pnas.2208792120
14. Piroska L, Fenyi A, Thomas S *et al.* Alpha-synuclein liquid condensates fuel fibrillar alpha-synuclein growth. *Sci Adv* 2023;**9**:33. https://doi.org/10.1126/sciadv.adg5663
15. Siegert A, Rankovic M, Favretto F *et al.* Interplay between tau and α-synuclein liquid–liquid phase separation. *Protein Sci* 2021;**30**:1326–36. https://doi.org/10.1002/pro.4025
16. Agarwal A, Chandran A, Raza F *et al.* VAMP2 regulates phase separation of alpha-synuclein. *Nat Cell Biol* 2024;**26**:1296–1308. https://doi.org/10.1038/s41556-024-01451-6
17. Sansevrino R, Hoffmann C, Milovanovic D. Condensate biology of synaptic vesicle clusters. *Trends Neurosci* 2023;**46**:293–306. https://doi.org/10.1016/j.tins.2023.01.001
18. Hallacli E, Kayatekin C, Nazeen S *et al.* The Parkinson's disease protein alpha-synuclein is a modulator of processing bodies and mRNA stability. *Cell* 2022;**185**:2035–56. https://doi.org/10.1016/j.cell.2022.05.008
19. Roden C, Gladfelter AS. RNA contributions to the form and function of biomolecular condensates. *Nat Rev Mol Cell Biol* 2020;**22**:183–95. https://doi.org/10.1038/s41580-020-0264-6
20. Maharana S, Wang J, Papadopoulos DK *et al.* RNA buffers the phase separation behavior of prion-like RNA binding proteins. *Science* 2018;**360**:918–21. https://doi.org/10.1126/science.aar7366
21. Dhakal S, Mondal M, Mirzazadeh A *et al.* Alpha-Synuclein emulsifies TDP-43 prion-like domain—RNA liquid droplets to promote heterotypic amyloid fibrils. *Commun Biol* 2023;**6**:1227. https://doi.org/10.1038/s42003-023-05608-1
22. Lipiński WP, Visser BS, Robu I *et al.* Biomolecular condensates can both accelerate and suppress aggregation of alpha-synuclein. *Sci Adv* 2022;**8**:48. https://doi.org/10.1126/sciadv.abq6495
23. Matsuo K, Asamitsu S, Maeda K *et al.* RNA G-quadruplexes form scaffolds that promote neuropathological alpha-synuclein aggregation. *Cell* 2024;**187**:6835–48. https://doi.org/10.1016/j.cell.2024.09.037
24. Rupert J, Monti M, Zacco E *et al.* RNA sequestration driven by amyloid formation: the alpha synuclein case. *Nucleic Acids Res* 2023;**51**:11466–78. https://doi.org/10.1093/nar/gkad857
25. Hardenberg M, Horvath A, Ambrus V *et al.* Widespread occurrence of the droplet state of proteins in the human proteome.

Proc Natl Acad Sci 2020;**117**:33254–62. https://doi.org/10.1073/pnas.2007670117

26. Kar M, Dar F, Welsh TJ *et al.* Phase-separating RNA-binding proteins form heterogeneous distributions of clusters in subsaturated solutions. *Proc Natl Acad Sci* 2022;**119**:28. https://doi.org/10.1073/pnas.2202222119
27. Ray S, Mason TO, Boyens-Thiele L *et al.* Mass photometric detection and quantification of nanoscale alpha-synuclein phase separation. *Nat Chem* 2023;**15**:1306–16. https://doi.org/10.1038/s41557-023-01244-8
28. Ubbiali D, Fratini M, Piersimoni L *et al.* Direct observation of "elongated" conformational states in alpha-synuclein upon liquid–liquid phase separation. *Angew Chem Int Edition* 2022;**61**:e202205726. https://doi.org/10.1002/anie.202205726
29. Saraiva MA. Evidence of the existence of micellar-like aggregates for alpha-synuclein. *Int J Biol Macromol* 2021;**177**:392–400. https://doi.org/10.1016/j.ijbiomac.2021.02.150
30. Galvanetto N, Ivanović MT, Chowdhury A *et al.* Extreme dynamics in a biomolecular condensate. *Nature* 2023;**619**:876–83. https://doi.org/10.1038/s41586-023-06329-5
31. Kang M, Day CA, Kenworthy AK *et al.* Simplified equation to extract diffusion coefficients from confocal FRAP data. *Traffic* 2012;**13**:1589–600. https://doi.org/10.1111/tra.12008
32. Elson EL, Magde D. Fluorescence correlation spectroscopy. I. Conceptual basis and theory. *Biopolymers* 1974;**13**:1–27. https://doi.org/10.1002/bip.1974.360130102
33. He G, GrandPre T, Wilson H *et al.* Phase-separating pyrenoid proteins form complexes in the dilute phase. *Commun Biol* 2023;**6**:19. https://doi.org/10.1038/s42003-022-04373-x
34. Wen J, Hong L, Krainer G *et al.* Conformational expansion of tau in condensates promotes irreversible aggregation. *J Am Chem Soc* 2021;**143**:13056–64. https://doi.org/10.1021/jacs.1c03078
35. Wawrezinieck L, Rigneault H, Marguet D *et al.* Fluorescence correlation spectroscopy diffusion laws to probe the submicron cell membrane organization. *Biophys J* 2005;**89**:4029–42. https://doi.org/10.1529/biophysj.105.067959
36. Buttafava M, Villa F, Castello M *et al.* SPAD-based asynchronous-readout array detectors for image-scanning microscopy. *Optica* 2020;**7**:755. https://doi.org/10.1364/optica.391726
37. Slenders E, Castello M, Buttafava M *et al.* Confocal-based fluorescence fluctuation spectroscopy with a SPAD array detector. *Light Sci Appl* 2021;**10**:31. https://doi.org/10.1038/s41377-021-00475-z
38. Rossetta A, Slenders E, Donato M *et al.* The BrightEyes-TTM as an open-source time-tagging module for democratising single-photon microscopy. *Nat Commun* 2022;**13**:7406. https://doi.org/10.1038/s41467-022-35064-0
39. Hochmair J, Exner C, Franck M *et al.* Molecular crowding and RNA synergize to promote phase separation, microtubule interaction, and seeding of Tau condensates. *EMBO J* 2022;**41**:e108882. https://doi.org/10.15252/embj.2021108882
40. Perego E, Zappone S, Castagnetti F *et al.* Single-photon microscopy to study biomolecular condensates. *Nat Commun* 2023;**14**:8224. https://doi.org/10.1038/s41467-023-43969-7
41. Fahim LE, Marcus JM, Powell ND *et al.* Fluorescence lifetime sorting reveals tunable enzyme interactions within cytoplasmic condensates. *J Cell Biol* 2024;**224**:e202311105. https://doi.org/10.1083/jcb.202311105
42. Esbjörner E, Chan F, Rees E *et al.* Direct observations of amyloid β self-assembly in live cells provide insights into differences in the kinetics of Aβ(1–40) and Aβ(1–42) aggregation. *Chem Biol* 2014;**21**:732–42. https://doi.org/10.1016/j.chembiol.2014.03.014
43. Chen W, Young LJ, Lu M *et al.* Fluorescence self-quenching from reporter dyes informs on the structural properties of amyloid clusters formed *in vitro* and in cells. *Nano Lett* 2016;**17**:143–9. https://doi.org/10.1021/acs.nanolett.6b03686
44. Laine RF, Sinnige T, Ma KY *et al.* Fast fluorescence lifetime imaging reveals the aggregation processes of α-synuclein and polyglutamine in aging *Caenorhabditis elegans*. *ACS Chem Biol* 2019;**14**:1628–36. https://doi.org/10.1021/acschembio.9b00354
45. Tortarolo G, Zunino A, Piazza S *et al.* Compact and effective photon-resolved image scanning microscope. *Adv Photon* 2024;**6**:016003. https://doi.org/10.1117/1.ap.6.1.016003
46. Pan H, Xia Y, Qin M *et al.* A simple procedure to improve the surface passivation for single molecule fluorescence studies. *Phys Biol* 2015;**12**:045006. https://doi.org/10.1088/1478-3975/12/4/045006
47. Schindelin J, Arganda-Carreras I, Frise E *et al.* Fiji: an open-source platform for biological-image analysis. *Nat Methods* 2012;**9**:676–82. https://doi.org/10.1038/nmeth.2019
48. Slenders E, Perego E, Buttafava M *et al.* Cooled SPAD array detector for low light-dose fluorescence laser scanning microscopy. *Biophys Rep* 2021;**1**:100025. https://doi.org/10.1016/j.bpr.2021.100025
49. Donato M, Slenders E, Zunino A *et al.* BrightEyes-MCS: a control software for multichannel scanning microscopy. *J Open Source Softw* 2024;**9**:7125. https://doi.org/10.21105/joss.07125
50. Castello M, Tortarolo G, Coto Hernández I *et al.* Universal removal of anti-Stokes emission background in STED microscopy via FPGA-based synchronous detection. *Rev Sci Instrum* 2017;**88**:053701.
51. Wahl M, Gregor I, Patting M *et al.* Fast calculation of fluorescence correlation data with asynchronous time-correlated single-photon counting. *Opt Express* 2003;**11**:3583. https://doi.org/10.1364/oe.11.003583
52. Petrášek Z, Derenko S, Schwille P. Circular scanning fluorescence correlation spectroscopy on membranes. *Opt Express* 2011;**19**:25006. https://doi.org/10.1364/oe.19.025006
53. Nath S, Meuvis J, Hendrix J *et al.* Early aggregation steps in alpha-synuclein as measured by FCS and FRET: evidence for a contagious conformational change. *Biophys J* 2010;**98**:1302–11. https://doi.org/10.1016/j.bpj.2009.12.4290
54. Mučibabić M, Apetri MM, Canters GW *et al.* The effect of fluorescent labeling on α-synuclein fibril morphology. *Biochim Biophys Acta* 2016;**1864**:1419–27. https://doi.org/10.1016/j.bbapap.2016.07.007
55. Uversky VN, Li J, Fink AL. Evidence for a partially folded intermediate in alpha-synuclein fibril formation. *J Biol Chem* 2001;**276**:10737–44. https://doi.org/10.1074/jbc.m010907200
56. Joshi N, Basak S, Kundu S *et al.* Attenuation of the early events of alpha-synuclein aggregation: a fluorescence correlation spectroscopy and laser scanning microscopy study in the presence of surface-coated Fe3O4 nanoparticles. *Langmuir* 2015;**31**:1469–78. https://doi.org/10.1021/la503749e
57. Perego E, Reshetniak S, Lorenz C *et al.* A minimalist model to measure interactions between proteins and synaptic vesicles. *Sci Rep* 2020;**10**:21086. https://doi.org/10.1038/s41598-020-77887-1
58. Wilhelm BG, Mandad S, Truckenbrodt S *et al.* Composition of isolated synaptic boutons reveals the amounts of vesicle trafficking proteins. *Science* 2014;**344**:1023–8. https://doi.org/10.1126/science.1252884
59. Sabari BR, Dall'Agnese A, Boija A *et al.* Coactivator condensation at super-enhancers links phase separation and gene control. *Science* 2018;**361**:6400. https://doi.org/10.1126/science.aar3958
60. Ng XW, Bag N, Wohland T. Characterization of lipid and cell membrane organization by the fluorescence correlation spectroscopy diffusion law. *CHIMIA* 2015;**69**:112. https://doi.org/10.2533/chimia.2015.112
61. Snead WT, Jalihal AP, Gerbich TM *et al.* Membrane surfaces regulate assembly of ribonucleoprotein condensates. *Nat Cell Biol* 2022;**24**:461–70. https://doi.org/10.1038/s41556-022-00882-3
62. Banks DS, Fradin C. Anomalous diffusion of proteins due to molecular crowding. *Biophys J* 2005;**89**:2960–71. https://doi.org/10.1529/biophysj.104.051078

63. Axpe E, Chan D, Offeddu GS *et al.* A multiscale model for solute diffusion in hydrogels. *Macromolecules* 2019;**52**:6889–97. https://doi.org/10.1021/acs.macromol.9b00753
64. Van Treeck B, Protter DSW, Matheny T *et al.* RNA self-assembly contributes to stress granule formation and defining the stress granule transcriptome. *Proc Natl Acad Sci* 2018;**115**:2734–9. https://doi.org/10.1073/pnas.1800038115
65. Lin Y, Protter DW, Rosen M *et al.* Formation and maturation of phase-separated liquid droplets by RNA-binding proteins. *Mol Cell* 2015;**60**:208–19. https://doi.org/10.1016/j.molcel.2015.08.018
66. Hyman AA, Weber CA, Jülicher F. Liquid-liquid phase separation in biology. *Annu Rev Cell Dev Biol* 2014;**30**:39–58. https://doi.org/10.1146/annurev-cellbio-100913-013325
67. Lücking CB, Brice A. Alpha-synuclein and Parkinson's disease. *Cell Mol Life Sci* 2000;**57**:1894–908. https://doi.org/10.1007/pl00000671
68. Alberti S, Gladfelter A, Mittag T. Considerations and challenges in studying liquid-liquid phase separation and biomolecular condensates. *Cell* 2019;**176**:419–34. https://doi.org/10.1016/j.cell.2018.12.035
69. Lakowicz JR, Szmacinski H. Fluorescence lifetime-based sensing of pH, Ca^{2+}, K^+ and glucose. *Sensors Actuators B: Chemical* 1993;**11**:133–43. https://doi.org/10.1016/0925-4005(93)85248-9
70. Peng X, Yang Z, Wang J *et al.* Fluorescence ratiometry and fluorescence lifetime imaging: using a single molecular sensor for dual mode imaging of cellular viscosity. *J Am Chem Soc* 2011;**133**:6626–35. https://doi.org/10.1021/ja1104014
71. Gracia P, Polanco D, Tarancón-Díez J *et al.* Molecular mechanism for the synchronized electrostatic coacervation and co-aggregation of alpha-synuclein and tau. *Nat Commun* 2022;**13**:4586. https://doi.org/10.1038/s41467-022-32350-9
72. Vazquez DS, Toledo PL, Gianotti AR *et al.* Protein conformation and biomolecular condensates. *Curr Res Struct Biol* 2022;**4**:285–307. https://doi.org/10.1016/j.crstbi.2022.09.004
73. Makasewicz K, Schneider TN, Mathur P *et al.* Formation of multicompartment structures through aging of protein-RNA condensates. *Biophys J* 2025;**124**:115–24. https://doi.org/10.1016/j.bpj.2024.11.014
74. Michel CH, Kumar S, Pinotsi D *et al.* Extracellular monomeric tau protein is sufficient to initiate the spread of tau protein pathology. *J Biol Chem* 2014;**289**:956–67. https://doi.org/10.1074/jbc.m113.515445
75. Delli Ponti R, Marti S, Armaos A *et al.* A high-throughput approach to profile RNA structure. *Nucleic Acids Res* 2016;**45**:e35. https://doi.org/10.1093/nar/gkw1094
76. Zacco E, Graña-Montes R, Martin SR *et al.* RNA as a key factor in driving or preventing self-assembly of the TAR DNA-binding protein 43. *J Mol Biol* 2019;**431**:1671–88. https://doi.org/10.1016/j.jmb.2019.01.028
77. Vandelli A, Cid Samper F, Torrent Burgas M *et al.* The interplay between disordered regions in RNAs and proteins modulates interactions within stress granules and processing bodies. *J Mol Biol* 2022;**434**:167159. https://doi.org/10.1016/j.jmb.2021.167159
78. Zacco E, Kantelberg O, Milanetti E *et al.* Probing TDP-43 condensation using an *in silico* designed aptamer. *Nat Commun* 2022;**13**:3306. https://doi.org/10.1038/s41467-022-30944-x
79. Luige J, Armaos A, Tartaglia GG *et al.* Predicting nuclear G-quadruplex RNA-binding proteins with roles in transcription and phase separation. *Nat Commun* 2024;**15**:2585. https://doi.org/10.1038/s41467-024-46731-9
80. Zanzoni A, Marchese D, Agostini F *et al.* Principles of self-organization in biological pathways: a hypothesis on the autogenous association of alpha-synuclein. *Nucleic Acids Res* 2013;**41**:9987–98. https://doi.org/10.1093/nar/gkt794
81. Thangavelu L, Moglad E, Afzal M *et al.* Non-coding RNAs in Parkinson's disease: regulating SNCA and alpha-synuclein aggregation. *Pathology* 2024;**261**:155511. https://doi.org/10.1016/j.prp.2024.155511
82. Staderini T, Bigi A, Mongiello D *et al.* Biophysical characterization of full-length TAR DNA-binding protein (TDP43) phase separation. *Protein Sci* 2022;**31**:e4509. https://doi.org/10.1002/pro.4509
83. Ji Y, Li F, Qiao Y. Modulating liquid-liquid phase separation of FUS: mechanisms and strategies. *J Mater Chem B* 2022;**10**:8616–28. https://doi.org/10.1039/d2tb01688e
84. Banani SF, Rice AM, Peeples WB *et al.* Compositional control of phase-separated cellular bodies. *Cell* 2016;**166**:651–63. https://doi.org/10.1016/j.cell.2016.06.010
85. Vicidomini Lab. VicidominiLab/BrightEyes-TTM: v1.0. Zenodo, 2022. https://doi.org/10.5281/ZENODO.7064910

Received: January 2, 2025. **Revised:** April 7, 2025. **Editorial Decision:** April 8, 2025. **Accepted:** May 3, 2025